

Geometry- and Relation-Aware Diffusion for EEG Super-Resolution

Laura Yao^{1*}, Gengwei Zhang^{1*}, Moajjem Chowdhury², Yunmei Liu², and Tianlong Chen¹

¹ UNITES Lab, University of North Carolina at Chapel Hill ² MINDxAI Lab, Dept. of Industrial & Systems Engineering, University of Louisville, Louisville, KY, USA.

* Equal Contribution

Recent electroencephalography (EEG) spatial super-resolution (SR) methods, while showing improved quality by either directly predicting missing signals from visible channels or adapting latent diffusion-based generative modeling to temporal data, often lack awareness of physiological spatial structure, thereby constraining spatial generation performance. To address this issue, we introduce TopoDiff, a geometry- and relation-aware diffusion model for EEG spatial super-resolution. Inspired by how human experts interpret spatial EEG patterns, TopoDiff incorporates topology-aware image embeddings derived from EEG topographic representations to provide global geometric context for spatial generation, together with a dynamic channel-relation graph that encodes inter-electrode relationships and evolves with temporal dynamics. This design yields a spatially grounded EEG spatial super-resolution framework with consistent performance improvements. Across multiple EEG datasets spanning diverse applications, including SEED/SEED-IV for emotion recognition, PhysioNet motor imagery (MI/MM), and TUSZ for seizure detection, our method achieves substantial gains in generation fidelity and leads to notable improvements in downstream EEG task performance.

1 Introduction

Electroencephalography (EEG) provides a noninvasive window into distributed cortical dynamics of brain and is widely used across affective computing (Zheng and Lu, 2015; Zheng et al., 2018; Chen et al., 2023), brain–computer interfaces (BCIs) (Goldberger et al., 2000; Schalk et al., 2004; Cho et al., 2017), and clinical neurophysiology such as epilepsy diagnosis (Herman et al., 2015; Waak et al., 2023).

Despite its broad applicability, standard EEG acquisition typically requires dense electrode placement over the scalp, which introduces hardware constraints and user discomfort, thereby limiting its use in out-of-lab scenarios. In contrast, low-density recording systems, such as wearable EEG devices, enable practical and longitudinal monitoring (Biondi et al., 2024; Cho et al., 2025; Vincenzo et al., 2025; Markov et al., 2024). However, these systems rely on sparse electrode layouts that discard fine-grained spatial information, leading to reduced performance in downstream analysis.

This gap has driven increasing interest in EEG spatial super-resolution (EEG SR) (Courellis et al., 2016; Corley and Huang, 2018; Svantesson et al., 2021), which aims to generate high-density EEG signals from sparse recordings. More recently, STAD (Wang et al., 2024a) employs a latent diffusion model to generate missing channels, while ESTFormer (Li et al., 2025) directly predicts missing signals using a masked autoencoder (He et al., 2022). However, as shown in Figure 1(a), these methods encode spatial information only implicitly through positional embeddings, which limits their ability to represent rich scalp geometry and to model structured cross-channel dependencies.

These observations motivate explicitly modeling electrode geometry and structured inter-channel relationships, rather than treating spatial positions as passive metadata. In clinical practice, EEG channels are rarely interpreted in isolation; instead, EEG signals are often summarized using *topographic maps*

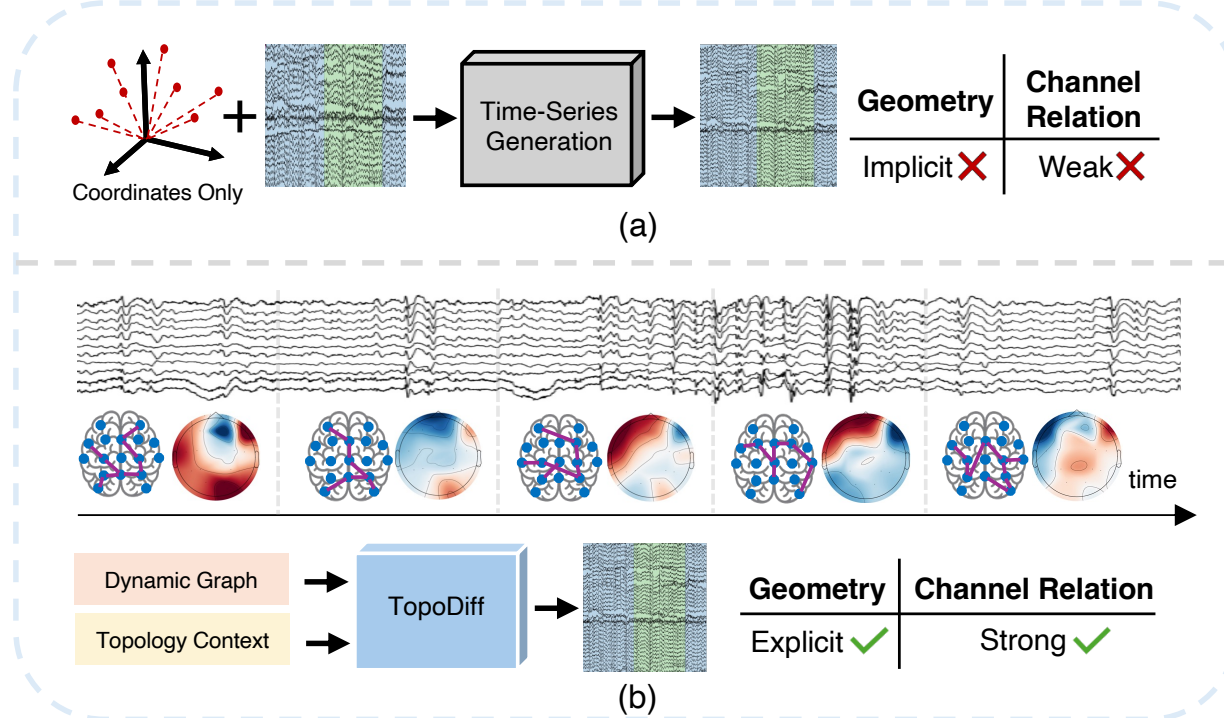


Figure 1: Comparison between previous pipelines and the proposed framework. (a) Prior methods only implicitly encode spatial geometry through coordinates and positional encoding. (b) **TopoDiff** enables geometry- and relation-aware generation by explicitly incorporating spatial and relational modeling.

(topoplots), which visualize the spatial distribution of signal amplitudes over the scalp (Koles and Paranjape, 1988). Such representations provide a global, geometry-aware view that highlights spatial organization and overall patterns, and naturally generalize across different electrode montages. This perspective suggests a complementary inductive bias for EEG spatial super-resolution: leveraging topographic representations to provide global spatial context. Moreover, electrode distributions can be naturally modeled using graph structures, which enable more structured and relational representations than treating channels as independent signals (Kotoge et al., 2025).

Building on these insights, as shown in Figure 1(b), we propose **TopoDiff**, a spatially grounded EEG SR framework that jointly leverages two structured representations: (i) **topology-aware image representations** derived from EEG topographic visualizations, which provide global scalp geometry context; and (ii) **dynamic channel-relation graphs** that model time-varying cross-channel dependencies. Building on recent advances in conditional diffusion models (Esser et al., 2024), we formulate EEG spatial super-resolution as a conditional generation problem, where high-density EEG signals are reconstructed by conditioning on both geometric and relational cues.

Our core contributions are summarized as follows:

- We propose a unified geometry- and relation-aware diffusion framework for EEG spatial super-resolution.
- We introduce **topology-aware modeling** via EEG topographic image embeddings to capture global scalp geometry alongside **relation-aware modeling** via channel-relationship graphs to encode structured and time-varying inter-channel dependencies, enabling generation of fine-grained spatiotemporal EEG patterns.
- Extensive experiments on SEED, SEED-IV, TUSZ, and PhysioNet MI/MM demonstrate improved reconstruction fidelity and stronger downstream performance compared to competitive baselines.

2 Related Work

Conditional Diffusion Methods. Conditional generation enables data synthesis guided by rich contextual information, ranging from class labels (Peebles and Xie, 2023), input signals (Wang et al., 2024a) to auxiliary modalities (Esser et al., 2024; Wan et al., 2025; Wei et al., 2025). Recently, diffusion models have emerged as a dominant paradigm for conditional generation due to their strong modeling flexibility and high sample quality (Dhariwal and Nichol, 2021; Ho, 2022; Saharia et al., 2022; Rombach et al., 2022; Esser et al., 2024; Wan et al., 2025). Motivated by this success, we adopt diffusion models for EEG SR and incorporate structured, domain-specific priors as conditioning guidance, rather than relying solely on signal-level inputs.

Generative Models for Time Series and EEG Super-Resolution. Generative modeling for time series has been widely explored for data augmentation (Shu et al., 2025), privacy-preserving synthesis (Tian et al., 2024), and probabilistic forecasting or imputation (Tashiro et al., 2021), with prominent model families including VAEs, GANs (Yoon et al., 2019), and, more recently, diffusion models for uncertainty-aware conditional generation (Rasul et al., 2021) (e.g., RDPI improves spatiotemporal imputation via a two-stage deterministic–diffusion framework (Liu et al., 2025b)). When applied to EEG, generative models have primarily been used for signal synthesis and data augmentation to mitigate data scarcity, but they typically operate on discrete channel tensors and encode electrode layout only implicitly, without explicitly modeling montage geometry (Shu et al., 2025; Williams et al., 2025). Recent EEG SR baselines adapt sequence models or diffusion frameworks specifically for spatial upsampling. ESTFormer (Li et al., 2025) employs Transformer attention with positional encodings and masking to reconstruct missing channels, while STAD (Wang et al., 2024a) and SRGDiff (Liu et al., 2025a) adopt diffusion-based generation with signal-derived conditioning and step-wise guidance. However, these methods largely rely on positional encodings and learn inter-channel relations implicitly within the model, which can overlook global scalp geometry and structured inter-electrode organization.

Downstream EEG Tasks. EEG has been used for tasks such as emotion recognition (Zheng and Lu, 2015), motor imagery (MI) classification (Schalk et al., 2004), and seizure detection (Herman et al., 2015), which are commonly adopted to evaluate EEG signal representations. EEG-based emotion recognition (Zheng and Lu, 2015; Craik et al., 2019) depends on spatial characteristics such as frontal asymmetry and cross-regional connectivity, potentially impacting multiple regions of the brain, indicating that any degradation in spatial fidelity can affect performance. MI classification (Schirrmeister et al., 2017; Lawhern et al., 2018) decodes limb movement from EEG signals and is highly sensitive to the spatial characterization of sensorimotor rhythms, which low-density montage often fails to capture. Finally, seizure detection provides a clinically grounded downstream task that requires preservation of both localized and distributed pathological patterns. Epileptic activity may manifest as focal or generalized abnormalities (Shah et al., 2018), making it extremely important to have an accurate spatial and temporal characterization of EEG signals (Shoeb, 2009; Roy et al., 2019). Collectively, these tasks span affective computing, BCI, and clinical neurophysiology—motivating work in spatially-grounded EEG SR methods.

3 Preliminary

3.1 EEG Spatial Super-Resolution

Let $X^{\text{LR}} \in \mathbb{R}^{C_{\text{LR}} \times T}$ denote a low-resolution (sparse-montage) EEG segment with C_{LR} channels and T time steps, and let $X^{\text{HR}} \in \mathbb{R}^{C_{\text{HR}} \times T}$ denote the corresponding high-resolution EEG with C_{HR} channels recorded over the same time window. The EEG spatial super-resolution (EEG SR) task is defined as estimating $X^{\text{SR}} \in \mathbb{R}^{C_{\text{HR}} \times T}$ that approximates X^{HR} , given X^{LR} as input. Since the low-resolution channels correspond to a known subset of the high-resolution montage, we define the target as reconstructing the unobserved signals $X^{\text{Unseen}} \in \mathbb{R}^{C_{\text{Unseen}} \times T}$.

3.2 Denoising Diffusion Models

Diffusion models learn to generate data by reversing a gradual noising process, which can be interpreted from the perspective of ordinary differential equations (ODEs) (Song et al., 2020; Chen et al., 2018; Albergo et al., 2025). During training, a noisy input z is obtained by interpolating between the data distribution and a noise distribution as $z = ax + b\epsilon$, where $\epsilon \sim \mathcal{N}(0, \mathbb{I})$ and $x \sim p(\mathbf{X})$. For simplicity,

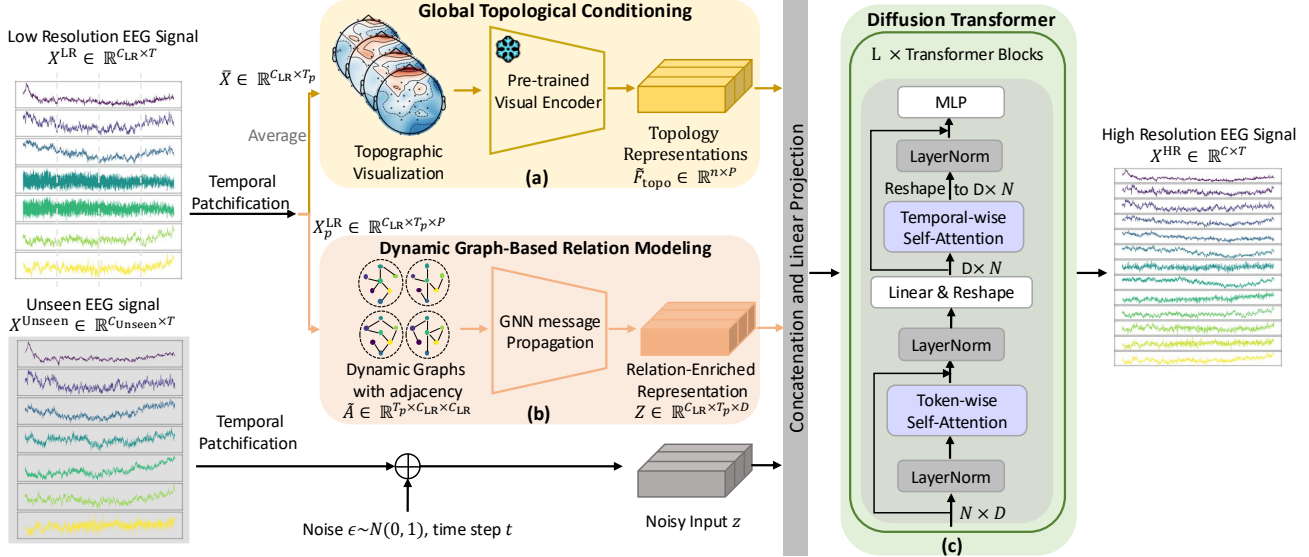


Figure 2: Overview of the **TopoDiff** framework. (a) Global topological conditioning, where EEG topographic representations are used to provide global scalp geometry and spatial context. (b) Dynamic graph-based inter-channel relation modeling, in which graphs are constructed in a time-varying manner and a GNN is used to enrich channel representations with explicit relational information. (c) The diffusion Transformer architecture employed for EEG spatial super-resolution.

following (Li and He, 2025), we use a linear noise schedule such that, given $t \in (0, 1)$, the noisy sample is obtained as $z = t x + (1 - t)\epsilon$. We adopt *x-prediction* (Li and He, 2025), where a denoising network f_θ directly predicts the clean signal at each t as $x_{\text{pred}} = f_\theta(z, t)$. In EEG spatial super-resolution, we formulate the task as a conditional generation problem, where noise is applied only to the unobserved channels, while the observed signals X^{LR} are provided as conditioning inputs throughout the diffusion process. Specifically, prediction is performed as $X_{\text{pred}}^{\text{Unseen}} = f_\theta(z, X^{\text{LR}}, t)$, and the model is trained with an ℓ_2 reconstruction loss, $\mathcal{L}_{\text{diff}} = \mathbb{E}_{x, \epsilon, t} \left[\|X_{\text{pred}}^{\text{Unseen}} - x^{\text{Unseen}}\|_2^2 \right]$.

At inference time, generation is performed by solving the reverse-time ODE conditioned on X^{LR} . Using *x*-prediction, the corresponding velocity field is given by $v_\theta(z, t) = \frac{x_{\text{pred}} - z}{t}$, yielding the ODE $\frac{dz}{dt} = v_\theta(z, t)$. Starting from Gaussian noise, the model iteratively denoises to obtain the generated unseen channels $X_{\text{gen}}^{\text{Unseen}}$.

4 TopoDiff Framework

The core idea of TopoDiff is to integrate geometric and relational inductive biases into the diffusion process in order to ensure spatially and temporally coherent EEG generation. We first describe the diffusion Transformer architecture used for EEG signal generation, and then introduce the global topological conditioning derived from EEG topographic representations, followed by the dynamic graph-based inter-channel relation modeling.

4.1 Diffusion Transformer Architecture

As illustrated in Figure 2, our model adopts a Transformer (Vaswani et al., 2017) architecture as the denoising generator. Given a low-resolution EEG input $X^{\text{LR}} \in \mathbb{R}^{C_{\text{LR}} \times T}$, we first partition the signal along the temporal dimension into non-overlapping patches, resulting in $X_p^{\text{LR}} \in \mathbb{R}^{C_{\text{LR}} \times T_p \times P}$, where P denotes the temporal patch size and $T_p = T/P$. We then merge the channel and patch-level temporal dimensions to obtain a sequence representation $X_c^{\text{LR}} \in \mathbb{R}^{N \times P}$, where $N = C_{\text{LR}} \times T_p$. This patchification and reshaping strategy enables the Transformer to jointly model spatial (channel-wise) and temporal

information within a unified sequence, analogous to spatiotemporal Transformer architectures commonly used in video processing and generation (Wan et al., 2025).

We apply the same patchification and reshaping procedure to the noisy input z , yielding $z_c \in \mathbb{R}^{N_z \times P}$, where $N_z = C_{\text{Unseen}} \times T_p$. The resulting z_c is concatenated with the conditional representation X_c^{LR} to form $X_c = [X_c^{\text{LR}}; z_c] \in \mathbb{R}^{(N+N_z) \times P}$. This concatenated sequence is then projected to a latent embedding $X_d \in \mathbb{R}^{(N+N_z) \times D}$ via a linear layer and provided as input to the Transformer, where D denotes the latent feature dimension.

Within each Transformer block, the architecture consists of two attention modules designed to capture spatiotemporal interactions: a token-wise self-attention layer and a temporal-wise self-attention layer. The token-wise self-attention operates over the full set of spatiotemporal tokens of size $N + N_z$, enabling global interactions across channels and time. In contrast, the temporal-wise self-attention first transposes the representation to a temporal-first form $X_t \in \mathbb{R}^{P \times (N+N_z)}$ and performs attention across elements within each temporal patch, facilitating local temporal modeling. After all Transformer blocks, a linear layer projects the features back to the shape of X_c , which is then reshaped to the original signal space to produce $X_{\text{pred}} \in \mathbb{R}^{C_{\text{HR}} \times T}$ and supervision is applied only to the unobserved channels.

4.2 Global Topological Conditioning

To provide the diffusion model with explicit global scalp geometry information, we incorporate high-level features extracted from EEG topographic representations as conditioning signals. These representations capture coarse-grained spatial organization across the entire scalp, providing global structural context that complements local channel-wise relational modeling. This design can be viewed as a form of cross-modal conditioning, in which image-based representations deterministically derived from EEG signals serve as auxiliary geometric priors to guide time-series generation.

Topographic Representation Construction. We leverage EEG topographic visualization images (Gramfort et al., 2013), which are constructed by interpolating EEG signals onto a two-dimensional projection of the scalp (Perrin et al., 1989; Koles and Paranjape, 1988). Such spatial visualizations are widely used by human experts in EEG analysis to reason about global spatial patterns.

First, low-resolution EEG input $\mathbf{X}^{\text{LR}} \in \mathbb{R}^{C_{\text{LR}} \times T}$ is partitioned along the temporal dimension into non-overlapping patches, $\mathbf{X}_p^{\text{LR}} \in \mathbb{R}^{C_{\text{LR}} \times T_p \times P}$, where P denotes the temporal patch size, chosen to be consistent with the Transformer configuration for simplicity. Within each temporal patch, a channel-wise temporal average operation is applied, obtaining $\bar{\mathbf{X}} \in \mathbb{R}^{C_{\text{LR}} \times T_p}$, which summarizes the dominant signal pattern within each time slot. Each averaged signal slice is then visualized as a color-coded two-dimensional EEG topographic image $\mathbf{I}_{\text{topo}} \in \mathbb{R}^{H \times W \times 3}$.

Global Feature Extraction and Conditioning. A frozen pretrained image feature extractor is applied to the topographic images to obtain a spatial feature map $\mathbf{F}_{\text{topo}} \in \mathbb{R}^{h \times w \times d}$, where h and w denote the spatial resolution of the extracted features and d is the feature dimension. We adopt the DINOv3 (Siméoni et al., 2025) model due to its strong pixel-level representation capability. The resulting features provide high-level spatial context derived from the EEG topographic representations.

Following conditioning strategies commonly adopted in conditional video generation models (Wan et al., 2025; Yang et al., 2024), we flatten the feature map and project it to the same latent dimension as the EEG token representations, yielding $\tilde{\mathbf{F}}_{\text{topo}} \in \mathbb{R}^{n \times D}$, where $n = h \times w$. This global topological embedding is concatenated with the EEG token sequence X_d at the beginning of the diffusion Transformer, serving as a global context that guides spatial channel generation throughout the diffusion process.

4.3 Dynamic Graph-Based Inter-Channel Relation Modeling

In addition to the diffusion process augmented with global spatial representations, we enhance relational modeling by introducing a dynamic graph neural network (GNN) that operates directly on the observed EEG channels. This module explicitly encodes time-varying cross-channel dependencies, facilitating more coherent multi-channel generation.

Group-wise Relation Estimation. Given the patchified input $X_p^{\text{LR}} \in \mathbb{R}^{C_{\text{LR}} \times T_p \times P}$, we estimate time-

varying inter-channel relations for each temporal group $X_p^{\text{LR}}(:, g, :)$, where $g \in \{0, \dots, T_p - 1\}$. Specifically, a dense and group-specific relation matrix $A^{(g)} \in \mathbb{R}^{C_{\text{LR}} \times C_{\text{LR}}}$ is computed using cosine similarity:

$$A_{ij}^{(g)} = \frac{\langle v_i^{(g)}, v_j^{(g)} \rangle}{\|v_i^{(g)}\| \|v_j^{(g)}\|}, \quad (4.1)$$

where $v_i^{(g)}$ denotes the input of channel i in group g . This group-wise relation estimation captures cross-channel dependencies that evolve over time.

Graph Construction. Given the group-wise relation matrix $A^{(g)}$, we construct a sparse, relation-aware graph for GNN processing. For each temporal group, the constructed graph nodes correspond to visible EEG electrodes, and spatial locality is imposed using the international 10–20 system (Klem et al., 1999). Each channel is connected to its n_s nearest neighbors according to electrode coordinates, forming an initial sparse topology. Edge weights are assigned based on the estimated relations by taking the absolute value of $A^{(g)}$ to allow both positive and negative correlations to contribute to relational strength: $\tilde{A}_{ij}^{(g)} = |A_{ij}^{(g)}|$. To control noise and avoid overly dense graphs, we retain only the top- k weighted edges per node.

Relation-Aware Channel Encoding with GNN. For each temporal group g , we first apply symmetric normalization to the adjacency matrix $\tilde{A}^{(g)}$ following the GCN formulation (Kipf, 2016) to ensure numerical stability:

$$\bar{A}^{(g)} = \left(D^{(g)}\right)^{-\frac{1}{2}} \tilde{A}^{(g)} \left(D^{(g)}\right)^{-\frac{1}{2}}, \quad (4.2)$$

where $\tilde{A}^{(g)} = \tilde{A}^{(g)} + \mathbb{I}$, and $D_{ii}^{(g)} = \sum_{j=1}^{C_{\text{LR}}} \tilde{A}_{ij}^{(g)}$.

Given the group-wise input $X^{(g)} = X_p^{\text{LR}}(:, g, :) \in \mathbb{R}^{C_{\text{LR}} \times P}$, we first project it to a D -dimensional channel embedding $\hat{X}^{(g)} \in \mathbb{R}^{C_{\text{LR}} \times D}$ using a linear layer. We then perform graph-based relation propagation as

$$X_1^{(g)} = \sigma(\bar{A}^{(g)} \hat{X}^{(g)} W_1), \quad (4.3)$$

$$X_2^{(g)} = \bar{A}^{(g)} X_1^{(g)} W_2, \quad (4.4)$$

$$Z^{(g)} = \hat{X}^{(g)} + X_2^{(g)}, \quad (4.5)$$

where $W_1, W_2 \in \mathbb{R}^{D \times D}$ are learnable projection matrices, $\sigma(\cdot)$ denotes a nonlinear activation (e.g., tanh), and the residual connection allows the module to function as a lightweight relational adapter that injects graph-structured interactions into the channel representations. Finally, the resulting relation-enriched features $Z \in \mathbb{R}^{C_{\text{LR}} \times T_p \times D}$ are subsequently fed into the Transformer layers, serving as relation-aware inputs in place of the raw EEG signals.

5 Experiments

5.1 Datasets and Preprocessing

We evaluate on four EEG benchmarks: **SEED** (Zheng and Lu, 2015; Duan et al., 2013) and **SEED-IV** (Zheng et al., 2018), **TUSZ** (TUH EEG Seizure Corpus) (Shah et al., 2018), and **PhysioNet MI/MM** (Schalk et al., 2004; Goldberger et al., 2000). SEED contains 62-channel EEG from 15 subjects with three emotion labels (positive/neutral/negative) sampled at 200 Hz, while SEED-IV extends this setup to four emotion categories. MI/MM comprises 64-channel EEG sampled at 160 Hz for specific limb movements, and TUSZ provides large-scale clinical scalp EEG for seizure detection with standard 10–20 montages (at least 19 channels) and sampling rates of at least 250 Hz. Collectively, these datasets span affective, motor, and clinical settings, enabling us to verify that the proposed method generalizes across diverse tasks and data collection conditions. For each dataset, we simulate wearable EEG configurations by subsampling channels from the original montage and treat the full montage as ground truth. Electrode coordinates are obtained from the standard international 10–20 system (Klem et al., 1999) and used

Table 1: Comparison of signal fidelity metrics across different datasets. Results are compared against recent baseline methods, including STAD (Wang et al., 2024a), RDPI (Liu et al., 2025b), and ESTFormer (Li et al., 2025), under $2\times$, $4\times$, and $8\times$ SR settings.

Method	2× SR			4× SR			8× SR		
	NMSE↓	SNR↑	PCC↑	NMSE↓	SNR↑	PCC↑	NMSE↓	SNR↑	PCC↑
SEED									
STAD (Wang et al., 2024a)	0.6780	1.689	0.530	0.7623	1.179	0.450	0.7517	0.697	0.359
RDPI (Liu et al., 2025b)	0.5667	2.470	0.667	0.6345	1.979	0.625	0.7238	1.406	0.544
ESTformer (Li et al., 2025)	0.5538	2.566	0.634	0.5499	2.597	0.635	0.6585	1.815	0.551
TopoDiff (Ours)	0.4982	3.026	0.674	0.5447	2.639	0.639	0.6303	2.004	0.574
SEED-IV									
STAD (Wang et al., 2024a)	0.4763	3.221	0.720	0.6555	1.834	0.559	0.7075	1.503	0.517
RDPI (Liu et al., 2025b)	0.3371	4.722	0.796	0.4117	3.854	0.730	0.4915	3.085	0.687
ESTformer (Li et al., 2025)	0.2648	5.770	0.840	0.3111	5.071	0.813	0.3912	4.076	0.765
TopoDiff (Ours)	0.2628	5.805	0.843	0.3091	5.099	0.814	0.3607	4.429	0.783
MI/MM									
STAD (Wang et al., 2024a)	0.5705	2.438	0.871	0.5985	2.229	0.875	0.6677	1.754	0.675
RDPI (Liu et al., 2025b)	0.1686	7.651	0.872	0.2132	6.712	0.851	0.3457	4.600	0.795
ESTformer (Li et al., 2025)	0.1788	7.477	0.902	0.2496	6.028	0.880	0.3085	5.108	0.845
TopoDiff (Ours)	0.1591	7.983	0.912	0.188	7.258	0.896	0.2326	6.334	0.871

to construct topology-aware spatial representations. We use subject-based train/test splits to ensure performance reflects cross-subject generalization rather than within-subject memorization.

Preprocessing. EEG data was first segmented into 4s then resampled to 200Hz (except for MI/MM in which we maintained the original 160Hz) to maintain homogeneity across all datasets. Then, a bandpass filter of 0-75Hz was applied to remove high frequency noise (Zheng and Lu, 2015). Finally, the amplitudes of the EEG segments were clamped to **200uv** in order to prevent extreme outliers and noise from impacting the model negatively.

Wearable Subsampling Protocol. We define super-resolution factors of $2\times$, $4\times$, and $8\times$ by selecting sparse subsets of channels from the full montage and reconstructing the full set. Unlike data-driven channel selection techniques that optimize for specific tasks (Tam et al., 2011; Gaur et al., 2021; Pane et al., 2018), the SR subsampling was done to ensure that the subsampled channels had adequate scalp coverage. The sampling followed the symmetrical positions commonly used in the 10-5, 10-10, and 10-20 systems (Michel and Murray, 2012), which ensure that the subsampled channels maintained adequate scalp coverage. With adequate scalp coverage corresponding to the underlying cortical regions, the selected channels can thus be used to capture the large-scale brain dynamics and distributed cortical activity (Jurcak et al., 2007). The channels selected using this paradigm are shown in the Appendix (Table 5).

5.2 Implementation Details

We implement our method with PyTorch, and all experiments are conducted on four NVIDIA RTX PRO 6000 GPUs. For all models, we use the AdamW optimizer with a learning rate of 5×10^{-4} and a weight decay of 0.01, together with a cosine learning rate scheduler. The diffusion Transformer consists of

Table 2: Comparison of signal fidelity metrics on TUSZ at $2\times$ super-resolution (SR). Metrics include signal fidelity (NMSE, SNR, PCC) and AUROC for seizure detection.

Method	NMSE↓	SNR↑	PCC↑	AUROC↑
Full Data	–	–	–	0.878
STAD	0.4519	3.450	0.634	0.540
RDPI	0.5263	2.790	0.701	0.551
ESTformer	0.36	4.437	0.732	0.855
TopoDiff (Ours)	0.3285	4.835	0.760	0.878

$L = 4$ layers with a hidden dimension of 800. Input signals are patchified with a patch size of $p = 50$ (and $p = 40$ for MI/MM to match the slightly different frequency), and all models are trained for 300 epochs. For global topological feature extraction, we adopt DINOv3 (Siméoni et al., 2025) and apply it to topographic visualizations constructed from temporally averaged EEG signals. For dynamic graph construction, we utilized $n_s = 12, k = 4$ for the $2\times$ factor and $n_s = 12, k = 6$ for $4\times$ and $8\times$ factors (further visualization in the Appendix).

5.3 Baselines

We compare against **ESTformer** (Li et al., 2025) and **STAD** (Wang et al., 2024a) as strong EEG super-resolution baselines, and include **RDPI** (Liu et al., 2025b) as a representative diffusion-based method for general spatiotemporal imputation. All methods are evaluated under identical super-resolution factors ($2\times, 4\times, 8\times$) using the same channel selections and identical subject-based train/test splits. We use the authors’ official implementations when available; otherwise, we provide faithful reimplementations and cross-check key architectural and training hyperparameters against the original papers.

For downstream evaluation, we adopt three recent EEG decoding models: **DMMR** (Wang et al., 2024b), **3D-CLMI** (Hao and Cheng, 2025), and **EvoBrain** (Kotoge et al., 2025), chosen as competitive, state-of-the-art baselines reported on the corresponding benchmarks. Using fixed downstream architectures isolates the effect of super-resolution quality, allowing us to quantify how improved reconstruction fidelity translates into gains in cross-subject decoding performance. This evaluation reflects common deployment scenarios where sparse wearable EEG is used for downstream inference, and improvements in super-resolution can translate into more reliable and generalizable predictions in real applications. For each of the baselines, we have trained models at each super-resolution factor (utilizing only the newly generated channels) to target the impact of our generated channels and how they perform in these scenarios.

5.4 Evaluation Metrics

We report both signal-level reconstruction fidelity and downstream task performance. Signal fidelity is measured using NMSE (normalized mean squared error; lower is better), SNR (signal-to-noise ratio between reconstructed and ground-truth signals; higher is better), and PCC (Pearson correlation coefficient capturing waveform similarity; higher is better). Specifically, we measure the fidelity of the unseen/generated channels for a better comparison on the results of the model. These metrics provide a decoder-agnostic assessment of super-resolution quality that is comparable across datasets and super-resolution factors.

For downstream evaluation, we quantify how reconstruction quality translates to end-task utility: emotion recognition on SEED/SEED-IV, movement (motor imagery) classification on PhysioNet MI/MM, and seizure detection on TUSZ. We report classification accuracy at each super-resolution factor ($2\times, 4\times, 8\times$). For TUSZ, since there are only 19 channels, we report metrics $2\times$ only as well as utilize AUROC for downstream task performance to better match metrics typically used for seizure detection (Kotoge et al., 2025).

5.5 Main Results

Table 1 and Table 2 summarize signal-level fidelity on SEED/SEED-IV, PhysioNet MI/MM, and TUSZ across multiple super-resolution (SR) factors. Across all datasets and SR levels, our TopoDiff framework achieves the best overall reconstruction quality, consistently improving NMSE, SNR, and PCC relative

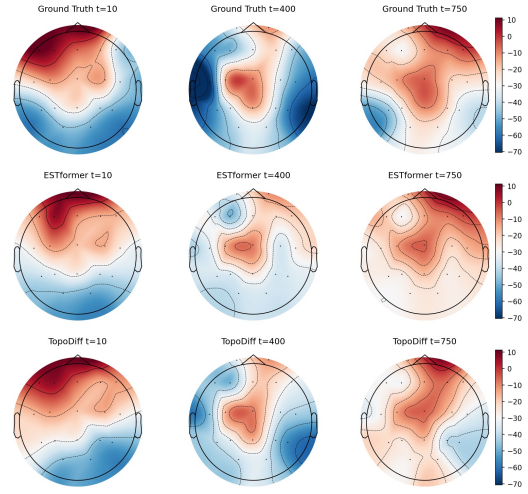


Figure 3: Topographical visualization of Ground Truth, ESTformer, and TopoDiff super-resolution outputs for the TUSZ $2\times$ setting at 3 different time steps.

Table 4: Downstream task accuracy (Acc) across datasets and super-resolution (SR) factors. Full Data denotes the use of real recordings (super-resolution training targets) for downstream evaluation.

Method	SEED (Emotion Recognition)			SEED-IV (Emotion Recognition)			PhysioNet MI/MM (Motor Imagery)		
	2× SR	4× SR	8× SR	2× SR	4× SR	8× SR	2× SR	4× SR	8× SR
Settings									
Full Data	0.5685	0.5726	0.5817	0.3068	0.3323	0.3322	0.6714	0.6924	0.6932
STAD	0.3523	0.4488	0.3361	0.2116	0.2217	0.2565	0.6428	0.6072	0.4267
RDPI	0.3496	0.4657	0.3386	0.2111	0.2151	0.2775	0.6569	0.6478	0.6110
ESTformer	0.3837	0.4309	0.3327	0.2109	0.2256	0.2885	0.6640	0.6424	0.5835
TopoDiff (Ours)	0.3845	0.4902	0.3890	0.2122	0.2272	0.2891	0.6701	0.6496	0.6155

to strong baselines (ESTformer, RDPI, STAD). The gains are most pronounced in the challenging 8× regime: compared to the best competing method, we improve SNR by **+10.4%** on SEED, **+8.7%** on SEED-IV, and **+24.0%** on MI/MM, alongside substantial NMSE reductions (e.g., MI/MM: 0.2326 vs. 0.3085). Lastly, as seen in Table 2, TopoDiff achieves the lowest NMSE and highest SNR/PCC, with a **+9.0%** increase in SNR overall.

Downstream Performance. Importantly, these signal-level gains translate into improved downstream decoding (Table 4). On SEED, TopoDiff shows its clearest advantage at 4× SR, improving accuracy from the best baseline 0.4657 to 0.4902 (**+5.3%** relative), and it remains stronger under the most aggressive setting at 8× SR (0.3890 vs 0.3386, **+14.9%**). Similarly, on PhysioNet MI/MM, TopoDiff is *competitive* at 2× SR (near full-data performance) and yields the best SR accuracy at 8× SR (0.6155 vs 0.6110, **+0.7%**). Overall, the pattern is that improvements become more pronounced as SR becomes harder, suggesting the model is not merely matching waveforms but preserving spatially structured, class-discriminative cues that matter for downstream inference under severe channel sparsity. Additionally, on TUSZ at 2× (Table 2), we also outperform prior methods on clinical utility, improving AUROC for seizure detection from 0.855 (ESTformer) to 0.878 (which matches the full data performance).

Visualization. Beyond quantitative gains, Figure 3 provides qualitative evidence that our reconstructions better preserve the spatial structure of the underlying EEG. The topographic maps show that TopoDiff reproduces regionally consistent patterns that more closely align with the Ground Truth, whereas ESTformer exhibits larger deviations in both the location and magnitude of activity. This closer agreement in spatial distribution suggests that TopoDiff recovers inter-channel relationships more faithfully, yielding signal distribution that are better matched to the original signals. More visualization can be found in the Appendix.

5.6 Ablation Studies

Effect of Graph Relation Modeling. Removing graph relation modeling causes a clear drop in reconstruction fidelity. As shown in Table 3, excluding the graph and relying only on topology conditioning (Diffusion + Topo) reduces SNR by 0.206, and similarly degrades NMSE and PCC. This suggests that the graph module provides essential dynamic inter-channel conditioning, enabling the diffusion model to capture time-varying electrode couplings that are not fully recoverable from global montage context alone.

Table 3: Ablation studies on the SEED dataset under the 2× super-resolution setting, including component-wise ablations (Topo: topological representation and Graph: graph-based relation modeling) and analyses of graph construction parameters.

Method	NMSE↓	SNR↑	PCC↑
Diffusion Baseline	0.5307	2.752	0.650
Diffusion + Topo	0.5224	2.820	0.656
Diffusion + Topo + Graph	0.4982	3.026	0.674
Diffusion + Graph ($n_s=12$, top- $k=4$)	0.5012	3.000	0.672
Diffusion + Graph ($n_s=14$, top- $k=8$)	0.5185	2.852	0.659
Diffusion + Graph ($n_s=6$, top- $k=\text{all}$)	0.5062	2.957	0.669

Effect of Topological Conditioning. As shown in the second row of Table 3, under the $2\times$ setting, incorporating topological conditioning improves the SNR by 0.07 and reduces the NMSE by 0.08, demonstrating its effectiveness in facilitating spatial generation. To further analyze how topological conditioning influences learning dynamics, we plot the validation SNR over the course of training in Figure 4. It can be observed that, with the global geometric prior provided by the topographic representations, the diffusion model converges significantly faster than the vanilla model. Owing to the global and smoothing characteristics of the topological representation, this conditioning encourages the model to capture spatial geometry early in training, leading to improved convergence behavior. Such behavior is consistent and significant across all super-resolution settings.

Impact of Different Sparsity Factors. We evaluate several sparsity settings for the two graph-pruning controls in our construction (Table 3). Overall, graph sparsity materially affects reconstruction quality: overly dense graphs can introduce noisy, weakly relevant couplings, while overly sparse graphs can remove informative spatial interactions, and both regimes degrade signal fidelity. Among the tested configurations, using a smaller neighbor set with a sufficiently rich candidate pool ($n_s=12$, top- $k=4$; see Sec. 4.3) yields the best performance compared to denser ($n_s=14$, top- $k=8$) or less selective ($n_s=6$, top- $k=\text{all}$) alternatives. Intuitively, this setting preserves adaptivity by allowing edge identities and weights to change across patches while still pruning enough, supporting the need to carefully control graph sparsity for stable, spatially consistent super-resolution.

6 Conclusion and Discussion

Our results highlight that *spatial representation* is a key bottleneck for EEG super-resolution. Rather than treating electrode coordinates as passive positional encodings, our approach conditions a diffusion model on **global topology-aware topoplot embeddings** and **channel-relationship graphs**, allowing the denoising process to jointly respect scalp geometry and structured inter-electrode dependencies. Additionally, we highlight the importance of dynamic conditioning for EEG time series which reflects the change in channel relationships across time. In the $2\times$, $4\times$, and $8\times$ super-resolution settings, we observe consistent gains in reconstruction quality and downstream decoding accuracy, indicating that the proposed dual conditioning remains effective as the upsampling task becomes more difficult.

Limitations and Future Work. Several directions could further extend this framework. First, while we use topoplot embeddings as a compact global geometric prior, richer subject-specific spatial cues (e.g., individualized electrode coordinates, head models, or montage calibration) may improve anatomical plausibility and cross-subject transfer, specifically allowing for better and more complete mapping to the brain. Second, our graph conditioning can be expanded to better capture state-dependent connectivity, for example by learning multi-scale or frequency-specific relational graphs and aligning them with known neurophysiological priors. Third, future work can leverage uncertainty for quality control (detecting unreliable reconstructions), active sensing (selecting which additional electrodes would most reduce uncertainty), or downstream-aware training (optimizing SR to maximize task performance). Finally, evaluating robustness under real-world noise, missing channels, and montage shifts enabling unified imputation, denoising, and cross-montage translation would broaden the practical impact of topology- and relation-grounded generative modeling for wearable EEG.

Acknowledgement

This research was partially funded by the National Institutes of Health (NIH) under award 1R01EB037101-01. The views and conclusions contained in this document are those of the authors and should not be interpreted as representing the official policies, either expressed or implied, of the NIH.

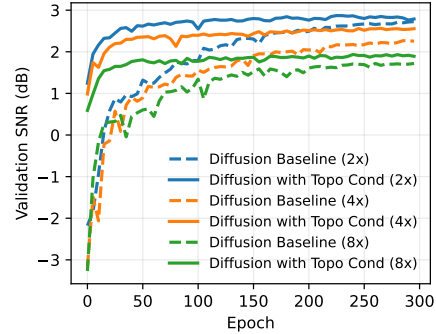


Figure 4: Convergence behavior with topological conditioning on the SEED dataset under $2\times$, $4\times$, and $8\times$ super-resolution settings.

References

Michael Albergo, Nicholas M Boffi, and Eric Vanden-Eijnden. Stochastic interpolants: A unifying framework for flows and diffusions. *Journal of Machine Learning Research*, 26(209):1–80, 2025. [3](#)

Andrea Biondi, Sara K. Simblett, Pedro F. Viana, Petroula Laiou, Anna M.G. Fiori, Ewan Nurse, Martijn Schreuder, Deb K. Pal, and Mark P. Richardson. Feasibility and acceptability of an ultra-long-term at-home eeg monitoring system (eeg@home) for people with epilepsy. *Epilepsy & Behavior*, 151: 109609, 2024. ISSN 1525-5050. doi: <https://doi.org/10.1016/j.yebeh.2023.109609>. URL <https://www.sciencedirect.com/science/article/pii/S1525505023005280>. [1](#)

Jingjing Chen, Xiaobin Wang, Chen Huang, Xin Hu, Xinken Shen, and Dan Zhang. A large finer-grained affective computing eeg dataset. *Scientific Data*, 10(1):740, Oct 2023. ISSN 2052-4463. doi: [10.1038/s41597-023-02650-w](https://doi.org/10.1038/s41597-023-02650-w). URL <https://doi.org/10.1038/s41597-023-02650-w>. [1](#)

Ricky TQ Chen, Yulia Rubanova, Jesse Bettencourt, and David K Duvenaud. Neural ordinary differential equations. *Advances in neural information processing systems*, 31, 2018. [3](#)

Hohyun Cho, Minkyu Ahn, Sangtae Ahn, Moonyoung Kwon, and Sung Chan Jun. Eeg datasets for motor imagery brain–computer interface. *GigaScience*, 6(7):gix034, 05 2017. ISSN 2047-217X. doi: [10.1093/gigascience/gix034](https://doi.org/10.1093/gigascience/gix034). URL <https://doi.org/10.1093/gigascience/gix034>. [1](#)

Jaeso Cho, Young Jun Ko, Yoon Gi Chung, Anna Cho, and Hunmin Kim. Improving epilepsy monitoring using long-term, in-home-bi-modal seizure monitoring device: clinical utilities and obstacles from a pilot study. *Frontiers in Neurology*, Volume 16 - 2025, 2025. ISSN 1664-2295. doi: [10.3389/fneur.2025.1609838](https://doi.org/10.3389/fneur.2025.1609838). URL <https://www.frontiersin.org/journals/neurology/articles/10.3389/fneur.2025.1609838>. [1](#)

Isaac A Corley and Yufei Huang. Deep eeg super-resolution: Upsampling eeg spatial resolution with generative adversarial networks. In *2018 IEEE EMBS international conference on biomedical & health informatics (BHI)*, pages 100–103. IEEE, 2018. [1](#)

Hristos S Courellis, John R Iversen, Howard Poizner, and Gert Cauwenberghs. Eeg channel interpolation using ellipsoid geodesic length. In *2016 IEEE biomedical circuits and systems conference (BioCAS)*, pages 540–543. IEEE, 2016. [1](#)

Alexander Craik, Yongtian He, and Jose L Contreras-Vidal. Deep learning for electroencephalogram (eeg) classification tasks: a review. *Journal of neural engineering*, 16(3):031001, 2019. [3](#)

Prafulla Dhariwal and Alex Nichol. Diffusion models beat gans on image synthesis. In *Proceedings of the 35th International Conference on Neural Information Processing Systems*, NIPS '21, 2021. ISBN 9781713845393. [3](#)

Ruo-Nan Duan, Jia-Yi Zhu, and Bao-Liang Lu. Differential entropy feature for EEG-based emotion classification. In *6th International IEEE/EMBS Conference on Neural Engineering (NER)*, pages 81–84. IEEE, 2013. [6, 16](#)

Patrick Esser, Sumith Kulal, Andreas Blattmann, Rahim Entezari, Jonas Müller, Harry Saini, Yam Levi, Dominik Lorenz, Axel Sauer, Frederic Boesel, et al. Scaling rectified flow transformers for high-resolution image synthesis. In *Forty-first international conference on machine learning*, 2024. [2, 3](#)

Pramod Gaur, Karl McCreadie, Ram Bilas Pachori, Hui Wang, and Girijesh Prasad. An automatic subject specific channel selection method for enhancing motor imagery classification in eeg-bci using correlation. *Biomedical Signal Processing and Control*, 68:102574, 2021. [7](#)

Ary L Goldberger, Luis AN Amaral, Leon Glass, Jeffrey M Hausdorff, Plamen Ch Ivanov, Roger G Mark, Joseph E Mietus, George B Moody, Chung-Kang Peng, and H Eugene Stanley. Physiobank, physiotoolkit, and physionet: components of a new research resource for complex physiologic signals. *circulation*, 101(23):e215–e220, 2000. [1, 6, 16](#)

Alexandre Gramfort, Martin Luessi, Eric Larson, Denis A Engemann, Daniel Strohmeier, Christian Brodbeck, Roman Goj, Mainak Jas, Teon Brooks, Lauri Parkkonen, et al. Meg and eeg data analysis with mne-python. *Frontiers in Neuroinformatics*, 7:267, 2013. 5

Yuejiang Hao and Shiwei Cheng. Motor imagery eeg classification method using 3d cnn and lstm for rehabilitation application. *Cognitive Neurodynamics*, 19(1):131, Aug 2025. 8

Kaiming He, Xinlei Chen, Saining Xie, Yanghao Li, Piotr Dollár, and Ross Girshick. Masked autoencoders are scalable vision learners. In *Proceedings of the IEEE/CVF conference on computer vision and pattern recognition*, pages 16000–16009, 2022. 1

Susan T. Herman, Nicholas S. Abend, Thomas P. Bleck, Kevin E. Chapman, Frank W. Drislane, Ronald G. Emerson, Elizabeth E. Gerard, Cecil D. Hahn, Aatif M. Husain, Peter W. Kaplan, Suzette M. LaRoche, Marc R. Nuwer, Mark Quigg, James J. Rivello, Sarah E. Schmitt, Liberty A. Simmons, Tammy N. Tsuchida, and Lawrence J. Hirsch. Consensus statement on continuous eeg in critically ill adults and children, part ii: Personnel, technical specifications, and clinical practice. *Journal of Clinical Neurophysiology*, 32(2), 2015. ISSN 0736-0258. URL https://journals.lww.com/clinicalneurophys/fulltext/2015/04000/consensus_statement_on_continuous_eeg_in.2.aspx. 1, 3

Jonathan Ho. Classifier-free diffusion guidance. *ArXiv*, abs/2207.12598, 2022. 3

Valer Jurcak, Daisuke Tsuzuki, and Ippeita Dan. 10/20, 10/10, and 10/5 systems revisited: their validity as relative head-surface-based positioning systems. *Neuroimage*, 34(4):1600–1611, 2007. 7

TN Kipf. Semi-supervised classification with graph convolutional networks. *arXiv preprint arXiv:1609.02907*, 2016. 6

George H. Klem, Hans Lüders, Herbert H. Jasper, and Christian Erich Elger. The ten-twenty electrode system of the international federation. the international federation of clinical neurophysiology. *Electroencephalography and clinical neurophysiology. Supplement*, 52:3–6, 1999. 6

Zoly J. Koles and R. B. Paranjape. Topographic mapping of the eeg: An examination of accuracy and precision. *Brain Topography*, 1(2):87–95, Dec 1988. ISSN 1573-6792. doi: 10.1007/BF01129173. URL <https://doi.org/10.1007/BF01129173>. 2, 5

Rikuto Kotoge, Zheng Chen, Tasuku Kimura, Yasuko Matsubara, Takufumi Yanagisawa, Haruhiko Kishima, and Yasushi Sakurai. Evobrain: Dynamic multi-channel EEG graph modeling for time-evolving brain networks. In *The Thirty-ninth Annual Conference on Neural Information Processing Systems*, 2025. 2, 8

Vernon J Lawhern, Amelia J Solon, Nicholas R Waytowich, Stephen M Gordon, Chou P Hung, and Brent J Lance. Eegnet: a compact convolutional neural network for eeg-based brain–computer interfaces. *Journal of neural engineering*, 15(5):056013, 2018. 3

Dongdong Li, Zhongliang Zeng, Zhe Wang, and Hai Yang. Estformer: Transformer utilising spatiotemporal dependencies for electroencephalogram super-resolution. *Knowledge-Based Systems*, 317:113345, 2025. 1, 3, 7, 8

Tianhong Li and Kaiming He. Back to basics: Let denoising generative models denoise. *arXiv preprint arXiv:2511.13720*, 2025. 4

Hongjun Liu, Leyu Zhou, Zijianghao Yang, and Chao Yao. Step-aware residual-guided diffusion for eeg spatial super-resolution. *ArXiv*, abs/2510.19166, 2025a. 3

Zijin Liu, Xiang Zhao, and You Song. Rdpi: a refine diffusion probability generation method for spatiotemporal data imputation. In *Proceedings of the Thirty-Ninth AAAI Conference on Artificial Intelligence and Thirty-Seventh Conference on Innovative Applications of Artificial Intelligence and Fifteenth Symposium on Educational Advances in Artificial Intelligence*, AAAI’25/IAAI’25/EAAI’25. AAAI Press, 2025b. ISBN 978-1-57735-897-8. doi: 10.1609/aaai.v39i12.33335. URL <https://doi.org/10.1609/aaai.v39i12.33335>. 3, 7, 8

Karmen Markov, Mohamed Elgendi, and Carlo Menon. Eeg-based headset sleep wearable devices. *npj Biosensing*, 1(1):12, Oct 2024. ISSN 3004-8656. doi: 10.1038/s44328-024-00013-y. URL <https://doi.org/10.1038/s44328-024-00013-y>. 1

Christoph M Michel and Micah M Murray. Towards the utilization of eeg as a brain imaging tool. *Neuroimage*, 61(2):371–385, 2012. 7

Evi Septiana Pane, Adhi Dharma Wibawa, and Mauridhi Hery Pumomo. Channel selection of eeg emotion recognition using stepwise discriminant analysis. In *2018 International Conference on Computer Engineering, Network and Intelligent Multimedia (CENIM)*, pages 14–19. IEEE, 2018. 7

William Peebles and Saining Xie. Scalable diffusion models with transformers. In *Proceedings of the IEEE/CVF international conference on computer vision*, pages 4195–4205, 2023. 3

François Perrin, Jacques Pernier, Olivier Bertrand, and Jean Francois Echallier. Spherical splines for scalp potential and current density mapping. *Electroencephalography and clinical neurophysiology*, 72(2):184–187, 1989. 5

Kashif Rasul, Calvin Seward, Ingmar Schuster, and Roland Vollgraf. Autoregressive denoising diffusion models for multivariate probabilistic time series forecasting. In *International Conference on Machine Learning*, 2021. URL <https://api.semanticscholar.org/CorpusID:231719657>. 3

Robin Rombach, Andreas Blattmann, Dominik Lorenz, Patrick Esser, and Bjorn Ommer. High-Resolution Image Synthesis with Latent Diffusion Models . In *2022 IEEE/CVF Conference on Computer Vision and Pattern Recognition (CVPR)*, pages 10674–10685, Los Alamitos, CA, USA, June 2022. IEEE Computer Society. doi: 10.1109/CVPR52688.2022.01042. URL <https://doi.ieee.org/10.1109/CVPR52688.2022.01042>. 3

Yannick Roy, Hubert Banville, Isabela Albuquerque, Alexandre Gramfort, Tiago H Falk, and Jocelyn Faubert. Deep learning-based electroencephalography analysis: a systematic review. *Journal of neural engineering*, 16(5):051001, 2019. 3

Chitwan Saharia, William Chan, Saurabh Saxena, Lala Lit, Jay Whang, Emily Denton, Seyed Kamyar Seyed Ghasemipour, Burcu Karagol Ayan, S. Sara Mahdavi, Raphael Gontijo-Lopes, Tim Salimans, Jonathan Ho, David J Fleet, and Mohammad Norouzi. Photorealistic text-to-image diffusion models with deep language understanding. In *Proceedings of the 36th International Conference on Neural Information Processing Systems*, NIPS '22, 2022. ISBN 9781713871088. 3

Gerwin Schalk, Dennis Mcfarland, Thilo Hinterberger, NR Birbaumer, and Jonathan Wolpaw. Bci2000: a general-purpose brain-computer interface (bci) system. *IEEE Trans. Biomed. Eng.*, 51:1034–, 07 2004. doi: 10.1109/TBME.2004.827072. 1, 3, 6, 16, 17

Robin Tibor Schirrmeister, Jost Tobias Springenberg, Lukas Dominique Josef Fiederer, Martin Glasstetter, Katharina Eggensperger, Michael Tangermann, Frank Hutter, Wolfram Burgard, and Tonio Ball. Deep learning with convolutional neural networks for eeg decoding and visualization. *Human brain mapping*, 38(11):5391–5420, 2017. 3

Vinit Shah, Eva Von Weltin, Silvia Lopez, James Riley McHugh, Lillian Veloso, Meysam Golmohammadi, Iyad Obeid, and Joseph Picone. The temple university hospital seizure detection corpus. *Frontiers in neuroinformatics*, 12:83, 2018. 3, 6, 16, 17

Ali Hossam Shoeb. *Application of machine learning to epileptic seizure onset detection and treatment*. PhD thesis, Massachusetts Institute of Technology, 2009. 3

Kai Shu, Le Wu, Yuchang Zhao, Aiping Liu, Ruobing Qian, and Xun Chen. Data augmentation for seizure prediction with generative diffusion model. *IEEE Transactions on Cognitive and Developmental Systems*, 17(3):577–591, 2025. doi: 10.1109/TCDS.2024.3489357. 3

Oriane Siméoni, Huy V Vo, Maximilian Seitzer, Federico Baldassarre, Maxime Oquab, Cijo Jose, Vasil Khalidov, Marc Szafraniec, Seungeun Yi, Michaël Ramamondjisoa, et al. Dinov3. *arXiv preprint arXiv:2508.10104*, 2025. 5, 8

Jiaming Song, Chenlin Meng, and Stefano Ermon. Denoising diffusion implicit models. *arXiv preprint arXiv:2010.02502*, 2020. 3

Mats Svantesson, Håkan Olausson, Anders Eklund, and Magnus Thordstein. Virtual eeg-electrodes: Convolutional neural networks as a method for upsampling or restoring channels. *Journal of Neuroscience Methods*, 355:109126, 2021. 1

Wing-Kin Tam, Zheng Ke, and Kai-Yu Tong. Performance of common spatial pattern under a smaller set of eeg electrodes in brain-computer interface on chronic stroke patients: a multi-session dataset study. In *2011 annual international conference of the IEEE engineering in medicine and biology society*, pages 6344–6347. IEEE, 2011. 7

Yusuke Tashiro, Jiaming Song, Yang Song, and Stefano Ermon. CSDI: Conditional score-based diffusion models for probabilistic time series imputation. In M. Ranzato, A. Beygelzimer, Y. Dauphin, P.S. Liang, and J. Wortman Vaughan, editors, *Advances in Neural Information Processing Systems*, volume 34, pages 24804–24816. Curran Associates, Inc., 2021. URL https://proceedings.neurips.cc/paper_files/paper/2021/file/cfe8504bda37b575c70ee1a8276f3486-Paper.pdf. 3

Muhang Tian, Bernie Chen, Allan Guo, Shiyi Jiang, and Anru R Zhang. Reliable generation of privacy-preserving synthetic electronic health record time series via diffusion models. *Journal of the American Medical Informatics Association*, 31(11):2529–2539, 09 2024. doi: 10.1093/jamia/ocae229. 3

Ashish Vaswani, Noam Shazeer, Niki Parmar, Jakob Uszkoreit, Llion Jones, Aidan N Gomez, Łukasz Kaiser, and Illia Polosukhin. Attention is all you need. *Advances in neural information processing systems*, 30, 2017. 4

Ronca Vincenzo, Cecchetti Marianna, Capotorto Rossella, Di Flumeri Gianluca, Giorgi Andrea, Germano Daniele, Borghini Gianluca, Babiloni Fabio, and Arico' Pietro. Beyond the lab: real-world benchmarking of wearable eegs for passive brain-computer interfaces. *Brain Informatics*, 13, 2025. URL <https://api.semanticscholar.org/CorpusID:284309128>. 1

Michaela Waak, Joshua Laing, Lakshmi Nagarajan, Nicholas Lawn, and A. Harvey. Continuous electroencephalography in the intensive care unit: A critical review and position statement from an australian and new zealand perspective. *Critical Care and Resuscitation*, 25:9–19, 03 2023. doi: 10.1016/j.ccrj.2023.04.004. 1

Team Wan, Ang Wang, Baole Ai, Bin Wen, Chaojie Mao, Chen-Wei Xie, Di Chen, Feiwu Yu, Haiming Zhao, Jianxiao Yang, et al. Wan: Open and advanced large-scale video generative models. *arXiv preprint arXiv:2503.20314*, 2025. 3, 5

Shuqiang Wang, Tong Zhou, Yanyan Shen, Ye Li, Guoheng Huang, and Yong Hu. Generative ai enables eeg super-resolution via spatio-temporal adaptive diffusion learning. *IEEE Transactions on Consumer Electronics*, 71:1034–1045, 2024a. 1, 3, 7, 8

Yiming Wang, Bin Zhang, and Yujiao Tang. Dmmr: Cross-subject domain generalization for eeg-based emotion recognition via denoising mixed mutual reconstruction. *Proceedings of the AAAI Conference on Artificial Intelligence*, 38(1):628–636, Mar. 2024b. doi: 10.1609/aaai.v38i1.27819. URL <https://ojs.aaai.org/index.php/AAAI/article/view/27819>. 8

Haoran Wei, Yaofeng Sun, and Yukun Li. Deepseek-ocr: Contexts optical compression. *arXiv preprint arXiv:2510.18234*, 2025. 3

Chad Williams, Daniel Weinhardt, Joshua Hewson, Martyna Beata Płomecka, Nicolas Langer, and Sebastian Musslick. Eeg-gan: A generative eeg augmentation toolkit for enhancing neural classification. *bioRxiv*, 2025. 3

Zhuoyi Yang, Jiayan Teng, Wendi Zheng, Ming Ding, Shiyu Huang, Jiazheng Xu, Yuanming Yang, Wenyi Hong, Xiaohan Zhang, Guanyu Feng, et al. Cogvideox: Text-to-video diffusion models with an expert transformer. *arXiv preprint arXiv:2408.06072*, 2024. 5

Jinsung Yoon, Daniel Jarrett, and Mihaela van der Schaar. Time-series generative adversarial networks. In H. Wallach, H. Larochelle, A. Beygelzimer, F. d'Alché-Buc, E. Fox, and R. Garnett, editors, *Advances in Neural Information Processing Systems*, volume 32. Curran Associates, Inc., 2019. URL https://proceedings.neurips.cc/paper_files/paper/2019/file/c9efe5f26cd17ba6216bbe2a7d26d490-Paper.pdf. 3

W. Zheng, W. Liu, Y. Lu, B. Lu, and A. Cichocki. Emotionmeter: A multimodal framework for recognizing human emotions. *IEEE Transactions on Cybernetics*, pages 1–13, 2018. ISSN 2168-2267. doi: 10.1109/TCYB.2018.2797176. 1, 6, 16

Wei-Long Zheng and Bao-Liang Lu. Investigating critical frequency bands and channels for EEG-based emotion recognition with deep neural networks. *IEEE Transactions on Autonomous Mental Development*, 7(3):162–175, 2015. doi: 10.1109/TAMD.2015.2431497. 1, 3, 6, 7, 16, 17

Appendix

A	Implementation Details	16
A.1	Dataset Details	16
A.2	Channel Selection	16
A.3	Graph Construction	16
B	Empirical Results	16

A Implementation Details

A.1 Dataset Details

SEED and SEED-IV. The SJTU Emotion EEG Dataset (**SEED**) (Zheng and Lu, 2015; Duan et al., 2013) is a standard benchmark for EEG-based emotion recognition. It contains recordings from 15 subjects watching emotion-eliciting video clips labeled with three emotional states: positive, neutral, and negative. EEG is collected using a 62-channel system following the international 10-20 electrode placement standard with a sampling rate of 200 Hz. **SEED-IV** (Zheng et al., 2018) extends SEED with four emotion categories (happiness, sadness, fear, and neutrality), while using the same acquisition setup as **SEED**.

Physionet MI/MM. The PhysioNet MI/MM dataset (Schalk et al., 2004; Goldberger et al., 2000) is a widely used benchmark for MI and motor execution research in EEG-based brain–computer interfaces. It consists EEG recordings from 109 subjects performing or imagining movements of the left hand, right hand, both hands, or both feet in response to visual cues, thus resulting in a three-class classification problem. EEG signals are recorded with a 64-channel international 10–20 montage at a sampling rate of 160 Hz.

TUSZ. TUSZ (Shah et al., 2018) is a large-scale clinical EEG dataset for seizure detection and classification, consisting of long-term scalp EEG recordings acquired during continuous clinical monitoring. Recordings follow standard clinical 10–20 electrode montages (at least 19 channels) with sampling rates of at least 250 Hz.

A.2 Channel Selection

Table 5 lists the original channels and the channels selected for SR tasks. The channels were selected to ensure that the scalp coverage remains similar to the original electrode configuration. As a result the channels maintain a symmetry. For TUSZ, only $2 \times$ SR is considered as it had 19 channels in the full configuration. Furthermore, Figure 5 visualizes the EEG channels in different configurations, showcasing the symmetric coverage of the scalp.

A.3 Graph Construction

Figure 6 and Figure 7 show visualizations of how the graphs may change over time patches, adding and removing different edges and shifting the weights of existing edges. Both figures map graph constructions for the SEED dataset at the $2 \times$ factor, meaning there are 32 visible channels to potentially map connections between. They both demonstrate our strongest parameter setting for SEED $2 \times$ which was $n_s = 12, k = 4$.

B Empirical Results

Figure 8 and Figure 9 further show some results from our super-resolution model when compared at specific time steps to the ground truth and other baseline model generated signals.

Table 5: Channels selected for SR task based on symmetric channel selection.

Dataset	All Channels	2× SR	4× SR	8× SR
Physionet MI/MM (Schalk et al., 2004)	Fp1, Fpz, Fp2, AF2, AF3, AFz, AF4, AF8, F7, F5, F3, F1, Fz, F2, F4, F6, F8, FT7, FC5, FC3, FC1, FCz, FC2, FC4, FC6, FT8, T7, C5, C3, C1, Cz, C2, C4, C6, T8, TP7, CP5, CP3, CP1, CPz, CP2, CP4, CP6, TP8, P7, P5, P3, P1, Pz, P2, P4, P6, P8, PO7, PO5, PO3, POz, PO4, PO6, PO8, O1, Oz, O2, Iz	Fp1, Fpz, Fp2, Fz, F3, F4, F7, F8, FC1, FC2, FC5, FC6, Cz, C3, C4, T7, T8, TP7, TP8, CP1, CP2, CP5, CP6, P7, P8, Pz, P3, P4, PO3, PO4, Oz, O1, O2	Fp1, Fpz, F7, F8, T7, T8, F3, F4, C3, C4, P3, C4, P3, P4, P7, P8, O1, O2	F3, F4, C3, C4, P3, P4, O1, O2
SEED/SEEDIV (Zheng and Lu, 2015)	Fp1, Fpz, Fp2, AF3, AF4, F7, F5, F3, F1, Fz, F2, F4, F6, F8, FT7, FC5, FC3, FC1, FCz, FC2, FC4, FC6, FT8, T7, C5, C3, C1, Cz, C2, C4, C6, T8, TP7, CP5, CP3, CP1, CPz, CP2, CP4, CP6, TP8, P7, P5, P3, P1, Pz, P2, P4, P6, P8, PO7, PO5, PO3, POz, PO4, PO6, PO8, CB1, O1, Oz, O2, CB2	Fp1, Fpz, AF3, AF4, F7, F3, F4, F8, FC1, FC2, FC5, FC6, Cz, C4, T7, C3, C4, T8, CP5, CP1, CP2, CP6, P7, P3, Pz, P4, P8, PO3, PO4, O1, Oz, O2	Fp1, Fpz, F7, F8, T7, T8, F3, F4, C3, C4, P3, C4, P3, P4, P7, P8, O1, O2	F3, F4, C3, C4, P3, P4, O1, O2
TUSZ (Shah et al., 2018)	Fp1, Fpz, Fp2, F3, F4, F7, F8, Fz, C3, C4, Cz, P3, P4, Pz, O1, O2, T3, T4, T5, T6	Fp1, Fpz, F3, F4, C3, C4, O1, O2, Cz	—	—

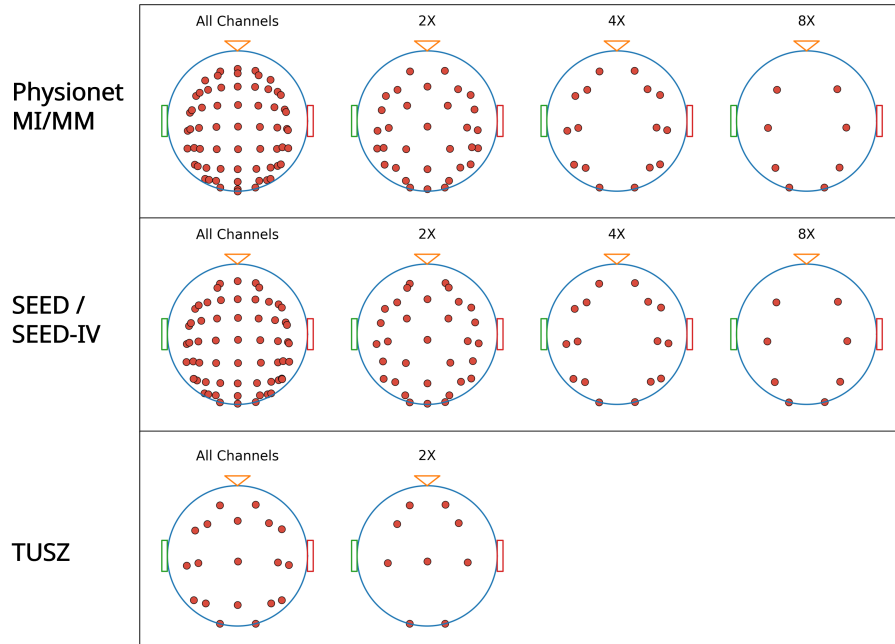


Figure 5: Visualization of EEG channels in full, 2× SR, 4× SR, and 8× SR configurations.

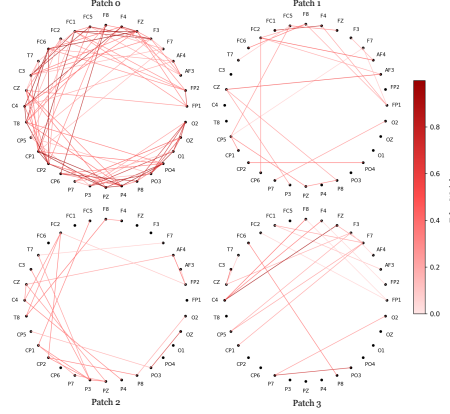


Figure 6: Examples of learned channel-relationship graphs with edge weights visualized by color intensity. The panels show the progression of a sample-specific connectivity pattern over the 10-20 montage at different temporal patches, showing only new edges when compared with the previous patch, highlighting how the relational graph adapts across time while preserving topology-consistent structure.

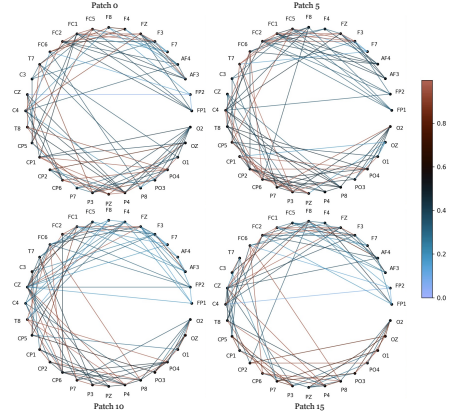


Figure 7: Graph construction over 4 temporal patches with $n_s = 12$ and $k = 4$ on the SEED 2 \times channel setting.

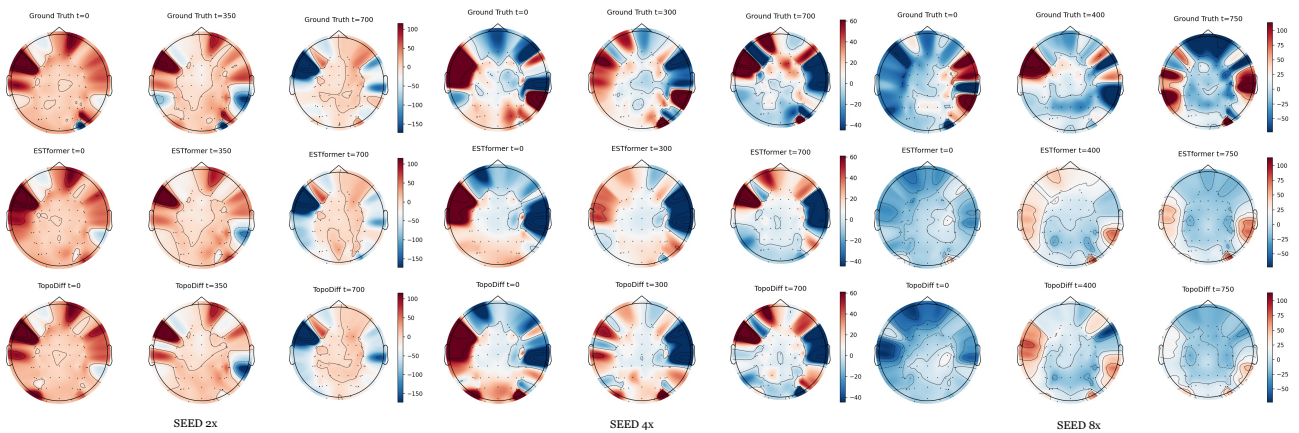


Figure 8: Topographical maps of Ground Truth, ESTformer, and TopoDiff HR outputs for different SEED settings at 3 different time steps.

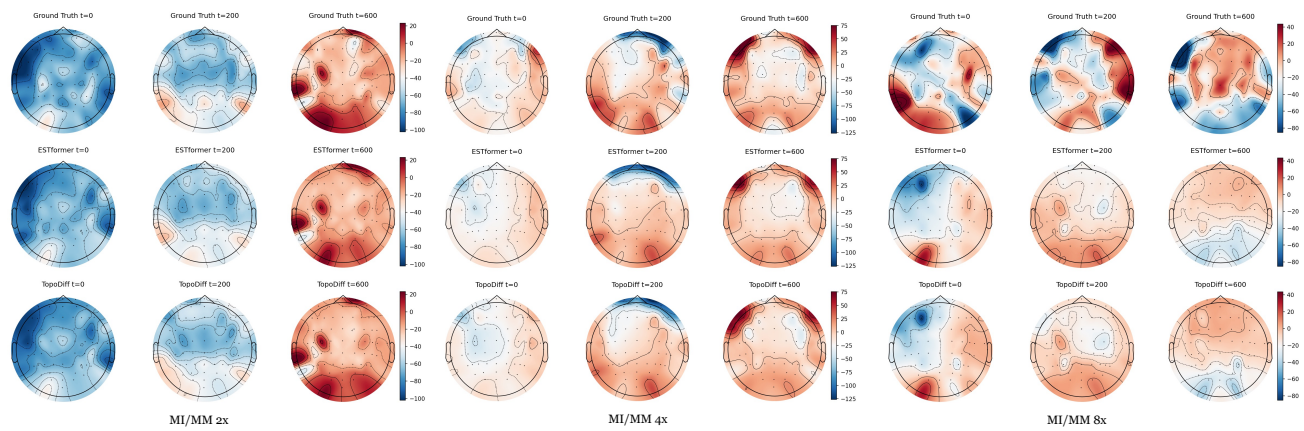


Figure 9: Topographical maps of Ground Truth, ESTformer, and TopoDiff HR outputs for different Physionet MI/MM settings at 3 different time steps.